Nonlocal self-organization of long stacking faults from highly strained nanocomposite film of complex oxide

Tomoya Horide,[1,*] Manabu Ishimaru,[1] Kazuhisa Sato,[2,†] and Kaname Matsumoto[1]

[1]*Department of Materials Science and Engineering, Kyushu Institute of Technology, 1-1 Sensui-cho, Tobata-ku, Kitakyushu 804-8550, Japan*

[2]*Institute for Materials Research, Tohoku University, 2-1 Katahira, Aoba-ku, Sendai 980-8577, Japan*

(Received 7 September 2018; revised manuscript received 5 November 2018; published 10 January 2019)

Elastic strain and defects are important key words for controlling structure and properties in films. While epitaxial strain and misfit dislocations have been discussed in conventional films, the evolution of strain and defect can be significantly varied by nanocomposite strain and complicated defects in oxides. In the present study, long stacking faults with a spacing of 5–30 nm and a length of >500 nm were self-organized by *ex situ* annealing highly strained nanocomposite films of $YBa_2Cu_3O_{7-\delta}$(YBCO) + $BaMO_3$ (M = Hf, Sn). It is surprising that the nonlocal nature of stacking faults, namely, the structural correlation over >500 nm, was observed in spite of the local configuration of the nanocomposite interface. This kind of structural variation was not observed in the pure YBCO film without nanorods, even when the same annealing was performed. A strain energy analysis showed that the stacking fault formation led to the strain energy minimum by reducing the nanocomposite strain. The layered structure of YBCO stacking faults and the large nanocomposite strain realized the present nonlocal self-organization, which is not observed in the conventional systems with epitaxial strain and misfit dislocations.

DOI: 10.1103/PhysRevMaterials.3.013403

I. INTRODUCTION

Strain has a significant influence on various properties of materials, and strain control is a very important topic for controlling functions of materials. Films including epitaxial, multilayer, and nanocomposite films are a very important system in strain engineering, since an interface fraction is large compared with a bulk system. Semiconducting epitaxial films are one of the most widely studied systems on this topic [1,2]. When a thin epitaxial film is deposited on a substrate, homogeneous elastic strain due to a lattice mismatch between substrate and film is accommodated in the film. If the thickness of a strained layer becomes large, misfit dislocations are formed to reduce the elastic strain energy [3]. Thus, competition between the elastic strain and the formation of misfit dislocations determines the film structure in semiconducting epitaxial films, and a desired strain situation is obtained by controlling this competition.

Oxide films are another important system of strain control since properties in oxides are significantly affected by strain [4,5]. The competition of elastic strain and misfit dislocations dominates the film structure also in oxide epitaxial films, as in the semiconducting epitaxial films. However, a characteristic structural nature is obtained in complex oxides: nanocomposite structure with high-density vertical interfaces [6] and complicated defects due to multiple components and complex crystalline structure. The elastic strain can be controlled using high-density vertical interfaces in the nanocomposite films. Elastic strain coupling at the interface between ferromagnetic and ferroelectric materials has realized multiferroics in $CoFe_2O_4 + BaTiO_3$ [7]; ferroelectric Curie temperature has been increased by elastic strain in the $BaTiO_3 + Sm_2O_3$ nanocomposite films [8]; and by analyzing structure, vertical strain control has been demonstrated in oxide in the nanocomposite films of $La_{0.7}Sr_{0.3}MnO_3 + ZnO$ and $BiFeO_3 + Sm_2O_3$ [9]. The elastic strain and misfit dislocation spacing along the vertical interface are determined by the strain energy minimization in the $YBa_2Cu_3O_7$ (YBCO) + $BaZrO_3$ (BZO) films as is discussed in semiconducting epitaxial films [10]. On the other hand, the multiple components and complex crystalline structure in complex oxides make defect structures of stacking faults [11,12], antiphase boundaries [13], and Ruddlesden-Popper defects [14], etc., complicated. An interaction of nanoparticles and twin boundaries has been reported in YBCO films [15]. These suggest that a characteristic situation of elastic strain and defects is realized in complex oxides if the nanocomposite strain and the complicated defects dominate the structural evolution.

In the present study, we demonstrate nonlocal self-organization resulting from the nanocomposite strain and complicated defects. To observe this, we selected the YBCO + $BaMO_3$(M = Hf, Sn; BMO) nanocomposite films with stacking faults for the following reasons: Large nanocomposite strain is achieved in the YBCO + BMO; the stacking faults in YBCO films are perpendicular to the nanocomposite interface, suggesting that the stacking fault formation is strongly affected by the vertical nanocomposite strain. The main result in the present study is the successful self-organization of long stacking faults, which is presented in Sec. III A. The mechanism of this self-organization will be clarified based on stacking fault energy (Sec. III B), elastic strain (Sec. III C), and interface structure (Sec. III D).

*horide@post.matsc.kyutech.ac.jp

†Present address: Research Center for Ultra-High Voltage Electron Microscopy, Osaka University, 7-1 Mihogaoka, Ibaraki, Osaka 567-0047, Japan.

II. EXPERIMENTAL PROCEDURE AND CALCULATION DETAILS

A. Sample preparation

Pure YBCO, YBCO + $BaSnO_3$(BSO), and YBCO + $BaHfO_3$ (BHO) films were prepared on $SrTiO_3$ (STO) (100) single-crystalline substrates using pulsed laser deposition (PLD), where pure YBCO target, mixed YBCO + BHO (4.7 vol %), and mixed YBCO + BSO (2.7 vol %) targets were ablated. The thickness was 150–210 nm for the YBCO + $BaMO_3$(M = Hf, Sn) and 250 nm for the pure YBCO. After the deposition, the YBCO films were cooled down to 200 °C in ∼30 min under an oxygen pressure of 5.5×10^4 Pa to oxidize the films. Properties of the films have been reported previously [16]. Some samples were *ex situ* annealed under oxygen flow at 450 °C for 1.5 h in a tube furnace, and cooled down to 300 °C to remove the samples from the furnace.

B. Structural evaluation

The microstructures of the specimens were characterized using a JEOL JEM-ARM200F scanning transmission electron microscope (STEM) operating at 200 kV with a CEOS aberration corrector for the probe-forming lens and a cold-field emission gun. We set the beam convergence to be ∼23 mrad in the semiangle. The high-angle annular dark-field (HAADF)–STEM images were acquired with the collection semiangle of 68–175 mrad. On the other hand, the cross-sectional bright-field transmission electron microscopy (TEM) images were taken by JEOL JEM-3000F device operating at 300 kV.

A 2θ-ω scan and reciprocal space mapping (RSM) were performed in x-ray diffraction (XRD) with Cu $K\alpha$ radiation ($\lambda = 1.5418$ Å). From the peaks in RSM, the lattice parameters were obtained: $a_{\mathrm{BMO}//} = a_{\mathrm{STO}}/|H|$, $a_{\mathrm{BMO}\perp} = a_{\mathrm{STO}}/(L/3)$, $a_{\mathrm{YBCO}} = a_{\mathrm{STO}}/|H|$, and $c_{\mathrm{YBCO}} = a_{\mathrm{STO}}/(L/8)$.

C. DFT calculation

A density functional theory (DFT) calculation was performed using the Vienna *Ab Initio* Simulation Package (VASP). The spin-polarized calculation for an O_2 molecule and the nonmagnetic calculation for the other systems were performed using the generalized gradient approximation (GGA) with an energy cutoff of 520 eV. The structure was relaxed until the force on the atoms became less than 0.02 eV/atom. To analyze the stacking fault energy ($\varepsilon_{\mathrm{SF}}$), we calculated a total energy for five systems: YBCO with stacking faults (n-YBCO/CuO/n-YBCO/CuO: $Y_{2n}Ba_{4n}Cu_{6n+2}O_{14n+2}$); YBCO with Cu-deficient stacking faults (YBCO/Cu_{1-x}O/YBCO/Cu_{1-x}O: $Y_2Ba_4Cu_{8-x}O_{16}$); Cu deficient YBCO; $(CuO)_2$; O_2. Since the $\varepsilon_{\mathrm{SF}}$ for $x = 0$ did not so significantly depend on the stacking fault spacing (YBCO thickness between stacking faults), the $\varepsilon_{\mathrm{SF}}$ was calculated for the YBCO/Cu_{1-x}O/YBCO/Cu_{1-x}O structure ($n = 1$). An x dependence of $\varepsilon_{\mathrm{SF}}$ was calculated in the YBCO/Cu_{1-x}O/YBCO/Cu_{1-x}O for $A = 4$ ($2a \times 2b \times c$ supercells) and $x = 0$–1/2 with $4 \times 4 \times 1$ Monkhorst-Pack k points. Here, A and x are the supercell size and the concentration of Cu deficiency in CuO chains, respectively. Assuming that the concentration of Cu deficiency was small, the lattice parameters of the YBCO with stacking faults were fixed at $a = 3.90$ Å, $b = 3.90$ Å, and $c = 27.63$ Å, which were obtained for the $Y_2Ba_4Cu_8O_{16}$($A = 1$, $x = 0$). For Cu deficient YBCO, a total energy was calculated for $2a \times 2b \times c$ ($y = 1/4$: $Y_4Ba_8Cu_{11}O_{28}$) and $3a \times 3b \times c$($y = 1/9$: $Y_9Ba_{18}Cu_{26}O_{63}$) supercells with $4 \times 4 \times 1$ and $3 \times 3 \times 1$ Monkhorst-Pack k points, respectively. Here, lattice parameters were fixed at those for the $YBa_2Cu_3O_7$, and only the atomic position was relaxed.

III. RESULTS

A. Self-organization of long stacking faults

Bright-field TEM images of the YBCO + BSO and YBCO + BHO films are shown in Fig. 1 to discuss the influence of annealing on a structure. Nanorods are elongated through the thickness of the film regardless of annealing, and the diameter and spacing are 10 and 40 nm for the YBCO + BSO and 7 and 20 nm for the YBCO + BHO. Long stacking faults were observed only in the annealed films, indicating that the *ex situ* annealing formed the stacking faults. A spacing of the long stacking faults along the c axis is 10–30 nm for the YBCO + BSO and 5–15 nm for the YBCO + BHO. This corresponds to the nonlocal self-organization, which is not observed in the conventional semiconducting films with epitaxial strain and misfit dislocations. It is surprising that the nonlocal nature of stacking faults, namely, the structural correlation over >500 nm, is observed in spite of the local configuration of the nanorod interface. The no-anneal films may contain "short" stacking faults which do not spread

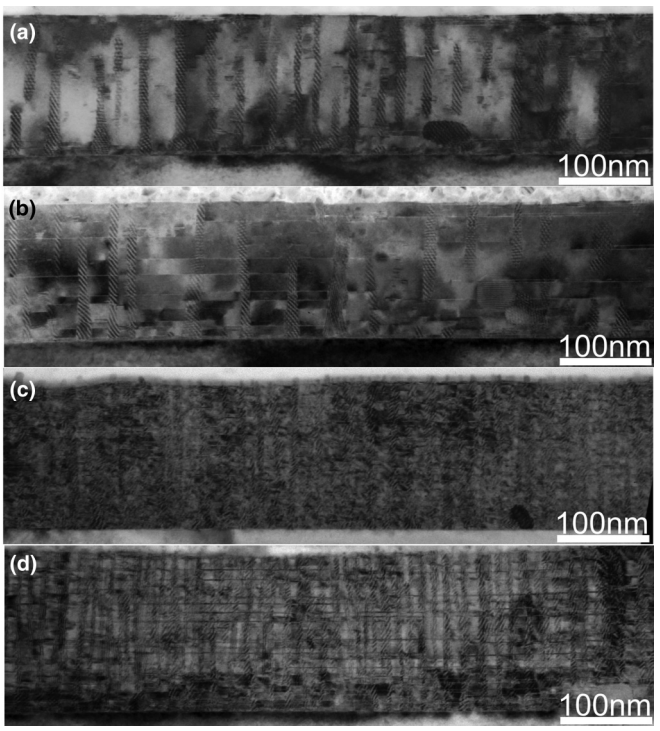

FIG. 1. Bright-field TEM images of (a) the no-anneal YBCO + BSO, (b) the annealed YBCO + BSO, (c) the no-anneal YBCO + BHO, and (d) the annealed YBCO + BHO films. The post–*ex situ* annealing formed the stacking faults in (b,d).

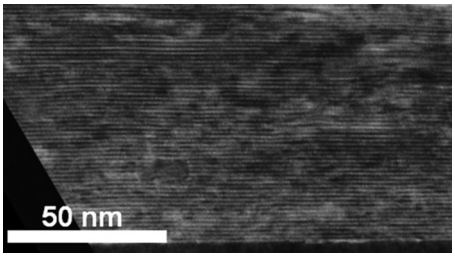

FIG. 2. Bright-field TEM image of the annealed pure YBCO film.

across several nanorods as shown in Figs. 1(a) and 1(c), but the length of stacking faults is significantly different between the no-anneal and annealed films. On the other hand, a TEM image of annealed pure YBCO film is shown in Fig. 2. The annealed pure YBCO film did not contain the stacking faults even when similar annealing was performed. The structural difference between the pure YBCO and YBCO + BMO films indicates that the nanorods significantly affected the defect formation in the YBCO + BMO films.

Figure 3(a) shows a HAADF-STEM image of the YBCO matrix in the annealed YBCO + BHO film to discuss the structure of the stacking faults at the atomic scale. The stacking structure of $Y/CuO_2/BaO/CuO/BaO/CuO_2$ is observed along the c axis, showing the YBCO structure in the film matrix. Additional CuO chains were inserted between the BaO plane and CuO chain, and the atomic planes shifted by 1/2 unit cell along the CuO chains (b axis), indicating the $YBa_2Cu_4O_8$-type stacking faults. The same type ($YBa_2Cu_4O_8$-type) stacking faults were observed also in the YBCO films prepared using the metal organic deposition (MOD) method [17]. A dark contrast suggests the Cu deficiencies in the stacking faults in Fig. 3(a). Similar Cu deficiencies in the $YBa_2Cu_4O_8$-type stacking faults have been observed in the MOD YBCO films by Gazquez *et al.* [18]. These show that the stacking faults comprising of the $Cu_{1-x}O$ chains were self-organized in the nanocomposite.

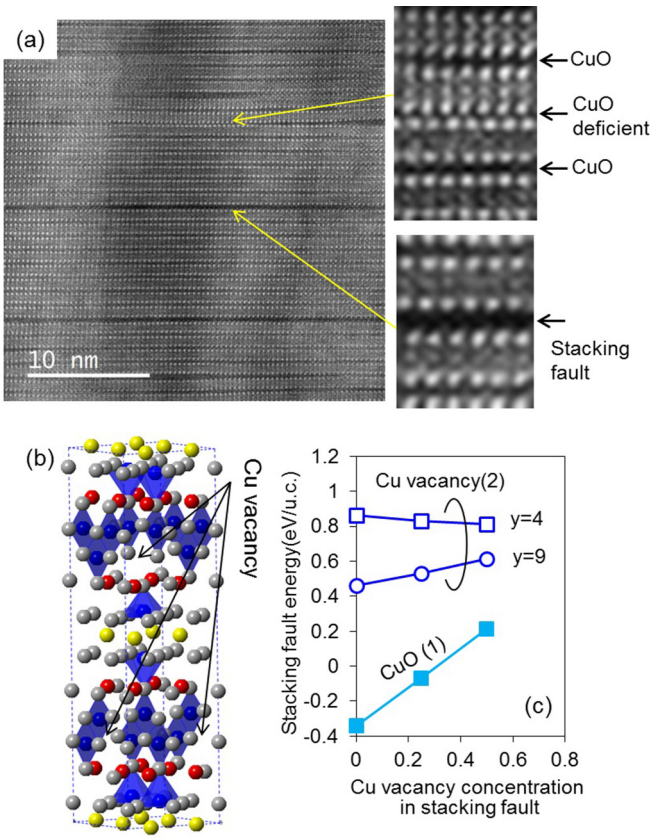

FIG. 3. HAADF-STEM image of the annealed YBCO + BHO(4.7) film. Enlarged views of the CuO-deficient layer (top right) and the $YBa_2Cu_4O_8$-type stacking faults (bottom right) are also shown. (b) The calculation model for Cu-deficient stacking fault [supercell size $(A) = 4$; concentration of Cu deficiencies $(x) = 2/8$; stacking fault spacing = 1 unit cell YBCO]. (c) Stacking fault energy [ε_{SF} for reactions (1a) and (2a)] as a function of the concentration of Cu deficiency in stacking fault.

B. Formation energy of stacking fault in the self-organization

Because the formation of the stacking faults requires additional $Cu_{1-x}O$ chains to YBCO, the mass conservation of Cu and O atoms should be considered. As for O atoms, the annealing under similar conditions significantly varies critical temperature, showing that O atoms are sufficiently supplied during the annealing [19]. As for the mass conservation of Cu, two Cu sources are considered in the present analysis. The Cu atoms are supplied to the stacking faults from (1) CuO precipitate in the no-anneal film, and (2) Cu vacancy formation in the YBCO matrix. A missing CuO layer in the YBCO matrix is observed in Fig. 2(a), suggesting that the reaction (2a) occurred at least in the region of Fig. 3(a). To discuss the stacking fault formation, a stacking fault energy [ε_{SF} (eV/unit cell), where unit cell = $a_{YBCO}b_{YBCO}$] was calculated using the DFT calculation considering two kinds of reactions. The calculation model of YBCO containing stacking faults ($Y_2Ba_4Cu_{6+2(1-x)}O_{16}$), namely the "product," is shown in Fig. 3(b), and the "reactant" (Cu source) is different between the following reactions.

First, the Cu supply from CuO precipitates is considered. The CuO precipitates supply the Cu atoms to form the $Cu_{1-x}O$ chains in the following reaction:

$$2AYBa_2Cu_3O_7 + 2A(1-x)CuO + AxO_2 \rightarrow AY_2Ba_4Cu_{6+2(1-x)}O_{16}, \tag{1a}$$

$$\Delta E(1a) = E[A(Y_2Ba_4Cu_{6+2(1-x)}O_{16})] - 2AE[YBa_2Cu_3O_7] - A(1-x)E[2(CuO)] - AxE[O_2], \tag{1b}$$

$$\varepsilon_{SF} = E(1a)/2A. \tag{1c}$$

$\Delta E(1a)$ denotes an energy variation in reaction (1a). The $A(Y_2Ba_4Cu_{6+2(1-x)}O_{16})$ contains stacking faults with an area of $2Aa_{YBCO}b_{YBCO}$, where a_{YBCO} and b_{YBCO} denote the a-axis length and b-axis length of YBCO. Here, $A = 4(2 \times 2 \times 1$ supercells) in the DFT calculation.

Second, the Cu supply by forming Cu vacancies in matrix is considered. The Cu atoms are supplied by forming the Cu deficiencies in YBCO matrix in the following reaction:

$$2A\mathrm{YBa_2Cu_3O_7} + 2A(1-x)/y\mathrm{YBa_2Cu_3O_7} + A\mathrm{O_2} \rightarrow A\mathrm{Y_2Ba_4Cu_{6+2(1-x)}O_{16}} + 2A(1-x)/y\mathrm{YBa_2Cu_{2+(1-y)}O_7}, \quad (2a)$$

$$\Delta E(2a) = E[\mathrm{A(Y_2Ba_4Cu_{6+2(1-x)}O_{16})}] + 2A(1-x)[1/y\mathrm{YBa_2Cu_{2+(1-y)}O_7}] - 2AE[\mathrm{YBa_2Cu_3O_7}] - 2A(1-x)/yE[\mathrm{YBa_2Cu_3O_7}] - AE[\mathrm{O_2}], \quad (2b)$$

$$\varepsilon_{\mathrm{SF}} = \Delta E(2a)/2A. \quad (2c)$$

In the DFT calculation, $A = 4(2 \times 2 \times 1$ supercells), and $y = 1/9(3 \times 3 \times 1$ supercells) or $1/4(2 \times 2 \times 1$ supercells).

Figure 3(c) shows a dependence of $\varepsilon_{\mathrm{SF}}$ on the Cu-deficiency concentration (x) for reactions (1a) and (2a). It is reasonable that the $\varepsilon_{\mathrm{SF}}$ increases with increase in the Cu deficiency because the stoichiometric $YBa_2Cu_4O_8$ phase is the most stable. From the DFT calculation, the $\varepsilon_{\mathrm{SF}}$ was estimated to be -0.3 to 0.6 eV/unit cell depending on the Cu source.

C. Reduction of elastic strain in the self-organization

Figure 4(a) shows 2θ-ω scan results in XRD in the no-anneal and annealed YBCO + BHO films. The STO(200), YBCO(005), and BHO(200) peaks are observed regardless of annealing. The *ex situ* annealing shifted the BHO(200) peak to low 2θ, and broadened the peak width of the BHO(200) and YBCO(005). Figures 4(b) and 4(c) show a RSM result in the no-anneal and annealed YBCO + BHO(4.7) films. In addition to the substrate peak of STO(103), YBCO(108) and BHO(103) peaks are observed in both the no-anneal and annealed films. The peak shift and peak broadening are also observed for the YBCO(108) and BHO(103) peaks. The broadening of the YBCO peak originated from the stacking faults which were observed in the TEM, and the peak shift suggests that the stacking fault formation strongly affected the elastic strain in the films. Figures 4(d) and 4(e) show the lattice parameters in the annealed YBCO + BHO(4.7) film, which are compared with those in the no-anneal YBCO + BHO films. The *ex situ* annealing, namely, the self-organization of stacking fault, decreased the elastic strain along the c axis. Similar peak shift and peak broadening by the *ex situ* annealing were observed also in the YBCO + BSO films (see Supplemental Material [21]).Thus, the peak broadening and shift in XRD demonstrate that the annealing varied the elastic strain and the stacking faults were formed.

D. Dislocation formation at interface in the self-organization

Figure 5 shows a HAADF-STEM image and geometric phase analysis (GPA) for the YBCO/BHO interface in the annealed YBCO + BHO(4.7) film to discuss the influence of strain on stacking fault formation at the atomic scale. Three stacking faults indicated by arrows are observed in the HAADF and GPA images. An inhomogeneous ε_{xx} is observed in the BHO nanorods due to defect formation caused by the atomic plane shift during the stacking fault formation. Dislocations are observed at the nanorod/matrix interface, and the spacing of dislocations is ~2.5 nm, which is

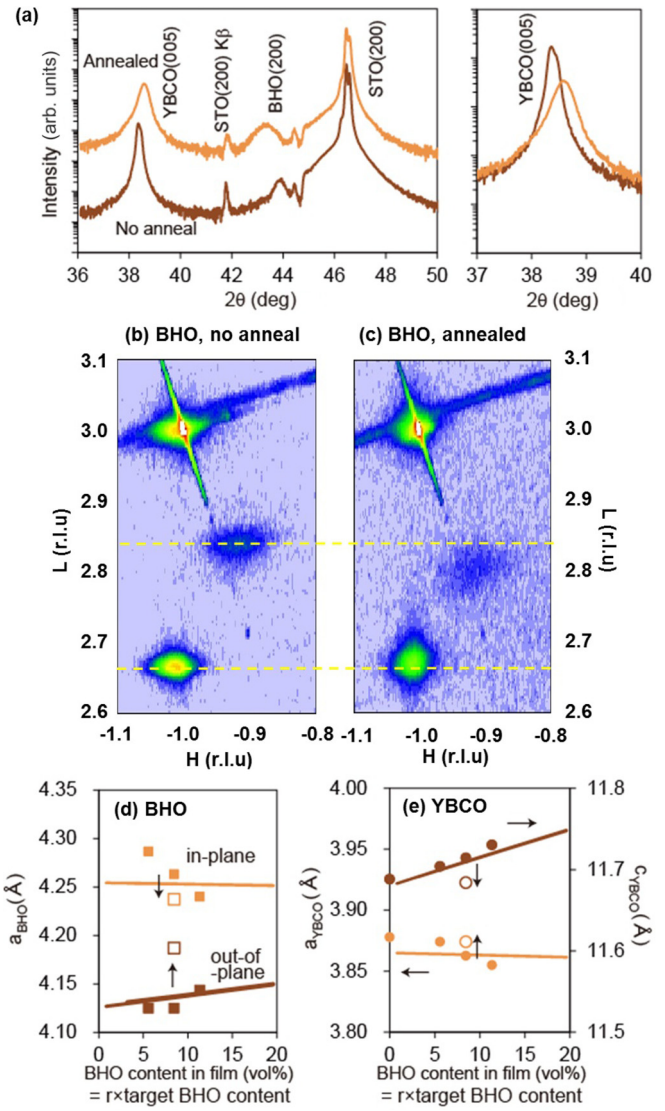

FIG. 4. (a) 2θ-ω scan results in the no-anneal and annealed YBCO + BHO(4.7) films. RSM results of the (b) no-anneal and (c) annealed YBCO + BHO(4.7) films. The reciprocal lattice unit (r.l.u) is defined with respect to the lattice parameter of STO ($a_{\mathrm{STO}} = 3.905$Å). BHO-content dependence of lattice parameters [(d) BHO, (e) YBCO] in the no-anneal and annealed YBCO + BHO films. Solid and open symbols denote the lattice parameters in the no-anneal and annealed film, respectively. The lines show the lattice parameters determined by elastic strain, which was calculated using the finite element method elastic calculation in [10,20]. $r = 1.9$ was obtained from the analysis.

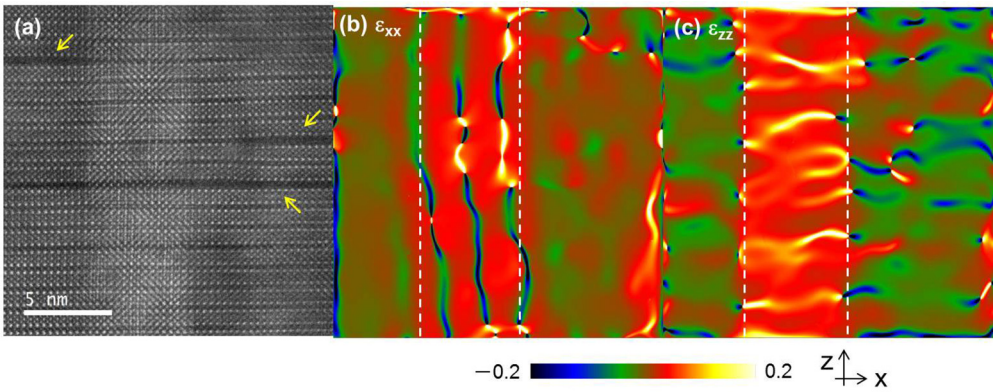

FIG. 5. (a) HAADF-STEM and GPA for (b) ε_{xx} and (c) ε_{zz} in the annealed YBCO + BHO(4.7) film. Dashed lines show the YBCO/BHO interface. Three stacking faults are observed as indicated by arrows in (a).

smaller than that of stacking faults and the previously observed dislocation spacing in the YBCO + BZO [10]. This shows that two types of dislocations exist at the interface: (1) the misfit dislocations remaining from the no-anneal film; (2) the dislocations accompanying in the stacking fault formation.

IV. DISCUSSION

Section III showed that the self-organization was dominated by (1) elastic strain, (2) stacking faults, and (3) accompanying dislocations. Before strain energy analysis, the correlation between these factors should be discussed; namely, the magnitude of the elastic strain and the density of the accompanying dislocation should be described by the density of the stacking fault. When a stacking fault intersects the nanorod interface, a dislocation loop is formed, showing that densities of the accompanying dislocation and stacking fault are the same. A relationship between the magnitude of the elastic strain and the stacking fault density is discussed in Sec. IV A. After that, the minimization of strain energy is discussed in Sec. IV B to understand the mechanism of self-organization.

A. Influence of stacking fault on elastic strain

Figure 4 suggests that the elastic strain in the no-anneal films was reduced by the stacking faults, showing their strong correlation in the self-organization. Here, the elastic strain reduced by the stacking fault formation is estimated. When stacking faults with a vertical spacing of h are formed, the number of atomic planes between the stacking faults is increased from $6h/c_{\mathrm{YBCO}}$ to $6h/c_{\mathrm{YBCO}}+1$. Therefore, the mismatch component reduced by the stacking fault (f_{SF}) is given by

$$f_{\mathrm{SF}} = \frac{6h/c_{\mathrm{YBCO}} + 1 - 6h/c_{\mathrm{YBCO}}}{6h/c_{\mathrm{YBCO}}} = \frac{c_{\mathrm{YBCO}}}{6h}. \tag{3}$$

Here, f_{elastic} (no anneal) and f_{elastic} (anneal) denote elastic components of mismatch before annealing and that after annealing (stacking fault formation), and they have a relationship of $f_{\mathrm{elastic}}(\mathrm{no\ anneal}) = f_{\mathrm{elastic}}(\mathrm{anneal}) + f_{\mathrm{SF}}$.

B. Analysis of energy regarding the self-organization

The strain energy regarding the self-organization is analyzed for the three important factors of (1) elastic strain, (2) stacking faults, and (3) accompanying dislocations, which are illustrated in Fig. 6(a). A region of energy analysis with a volume of $s \times s$ (square lattice) $\times\, t$ (thickness) contains one nanorod with a diameter of d, which is also schematically illustrated in Fig. 6(a). Here, s is equal to the spacing of nanorods, since the square lattice of $s \times s$ corresponds to the region occupied by one nanorod.

1. Elastic strain energy

An elastic strain energy after the stacking fault formation is given by

$$\begin{aligned} E_{\mathrm{elastic}} &= \frac{1}{2}E_{\mathrm{matrix}}{\varepsilon_{zz,\mathrm{matrix}}}^2\left(s^2 - \frac{\pi d^2}{4}\right)t \\ &\quad + \frac{1}{2}E_{\mathrm{nanorod}}{\varepsilon_{zz,\mathrm{nanorod}}}^2\left(\frac{\pi d^2}{4}\right)t \\ &= \frac{1}{2}E_{\mathrm{matrix}}\left[\frac{\varepsilon_{zz,\mathrm{matrix}}(\mathrm{no\ anneal})}{f_{\mathrm{elastic}}(\mathrm{no\ anneal})}f_{\mathrm{elastic}}(\mathrm{anneal})\right]^2 \\ &\quad \times \left(s^2 - \frac{\pi d^2}{4}\right)t + \frac{1}{2}E_{\mathrm{nanorod}} \\ &\quad \times \left[\frac{\varepsilon_{zz,\mathrm{nanorod}}(\mathrm{no\ anneal})}{f_{\mathrm{elastic}}(\mathrm{no\ anneal})}f_{\mathrm{elastic}}(\mathrm{anneal})\right]^2\left(\frac{\pi d^2}{4}\right)t. \end{aligned} \tag{4}$$

E_{matrix}(=185 GPa), E_{nanorod}, $\varepsilon_{zz,\mathrm{matrix}}$, $\varepsilon_{zz,\mathrm{nanorod}}$, s, d, and t are a Young's modulus of YBCO, a Young's modulus of BMO, an out-of-plane elastic strain of YBCO, an out-of-plane elastic strain of BMO, a nanorod spacing, a nanorod diameter, and a film thickness. Here, we assume $E_{\mathrm{nanorod}} = E_{\mathrm{BHO}} \sim E_{\mathrm{BZO}} = 240$ GPa. $f_{\mathrm{elastic}}(\mathrm{no\ anneal}) = 0.027$ was obtained from the analysis using the finite element method and XRD [10]. $\varepsilon_{zz,\mathrm{matrix}}(\mathrm{no\ anneal})/f_{\mathrm{elastic}}(\mathrm{no\ anneal})$ and $\varepsilon_{zz,\mathrm{nanorod}}(\mathrm{no\ anneal})/f_{\mathrm{elastic}}(\mathrm{no\ anneal})$ were obtained from the lattice parameter, c, in the no-anneal films using the method discussed in [10].

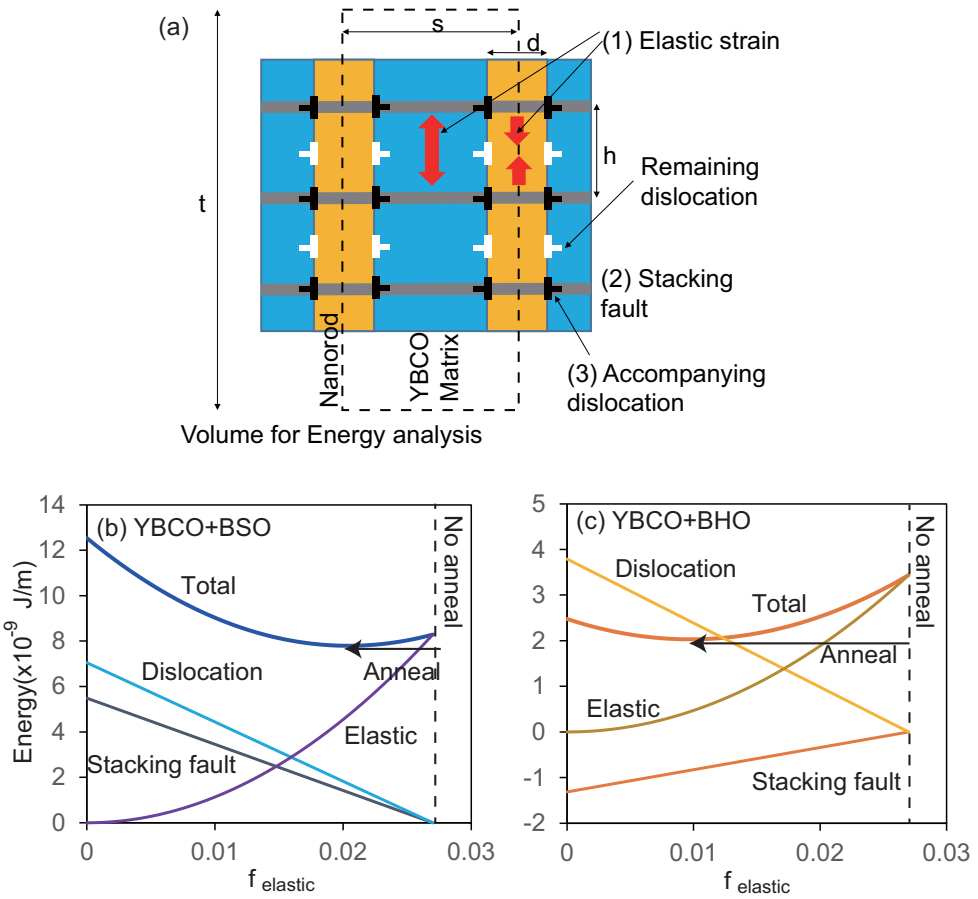

FIG. 6. (a) Schematic illustration of the important structural factors to determine the present film structure. Energy of dislocations, stacking faults, and elastic strain as a function of the elastic component in mismatch, f_{elastic} for (b) the YBCO + BSO and (c) the YBCO + BHO.

2. Stacking fault energy

According to Eq. (3), stacking fault spacing (h) is given by $h = c_{\text{YBCO}}/(6f_{\text{SF}})$. A stacking fault energy (E_{SF}) for the stacking faults with a spacing of h is given by

$$E_{\text{SF}} = \varepsilon_{\text{SF}} \frac{s^2}{a_{\text{YBCO}} b_{\text{YBCO}}} \frac{t}{h} = \varepsilon_{\text{SF}} \frac{s^2}{a_{\text{YBCO}} b_{\text{YBCO}}} \frac{6f_{\text{SF}}}{c_{\text{YBCO}}} t = \varepsilon_{\text{SF}} \frac{s^2}{a_{\text{YBCO}} b_{\text{YBCO}}} \times \frac{6[f_{\text{elastic}}(\text{no anneal}) - f_{\text{elastic}}(\text{anneal})]}{c_{\text{YBCO}}} t. \quad (5)$$

3. Dislocation energy

The misfit dislocations have already existed in the no-anneal films due to mismatch between YBCO and BMO [10]. However, because it is considered that the misfit dislocations remaining from the no-anneal films are not affected by the annealing, they are excluded from the present energy analysis. The dislocation energy (E_{dis}) for the accompanying dislocations is given by

$$E_{\text{dis}} = \frac{\mu |\boldsymbol{b}|^2}{4\pi(1-\nu)} \ln\left(\frac{R}{|\boldsymbol{b}|}\right) \times \pi d t \frac{6[f_{\text{elastic}}(\text{no anneal}) - f_{\text{elastic}}(\text{anneal})]}{c_{\text{YBCO}}}, \quad (6)$$

where $\mu = E/2(1+\nu)$, $R = (s/2 + d/2)/2$, $\boldsymbol{b}$ is the Burgers vector, and ν is the Poisson ratio. Here, the density of dislocation is the same as that of the stacking fault.

Figures 6(b) and 6(c) show $E_{\text{total}}(=E_{\text{elastic}} + E_{\text{SF}} + E_{\text{dis}})$, E_{elastic}, E_{SF}, and E_{dis} as a function of f_{elastic}(anneal) for the YBCO + BSO and the YBCO + BHO. Here, $|\boldsymbol{b}| = c_{\text{YBCO}}/6 = 0.19$ nm and $f_{\text{elastic}}(\text{no anneal}) = 0.027$. For $\varepsilon_{\text{SF}} = -0.02$ eV/u.c. (unit cell), $d = 7$ nm, and $s = 21$ nm [the parameters of the YBCO + BHO(4.7)], the energy is minimized at $f_{\text{elastic}}(\text{anneal}) = 0.01$. Similarly, for $\varepsilon_{\text{SF}} = 0.02$ eV/u.c., $d = 11$ nm and $s = 43$ nm [the parameters of the YBCO + BSO(2.7)], the energy is minimized at $f_{\text{elastic}}(\text{anneal}) = 0.021$. It follows that $h = c_{\text{YBCO}}/(6f_{\text{SF}}) = 11$ nm for the parameters of the YBCO + BHO(4.7), and $h = c_{\text{YBCO}}/(6f_{\text{SF}}) = 32$ nm for the parameters of the YBCO + BSO(2.7) (analysis of h_{SF} with varying the parameters is shown in the Supplemental Material [21]). The h values obtained in the energy analysis are consistent with the average spacing of stacking faults observed in the TEM.

The ε_{SF} values are discussed to confirm the validity of the present analysis. From the DFT calculation [Fig. 3(c)], we confirm that the ε_{SF} is in a reasonable range. The ε_{SF} for YBCO + BHO(4.7) was smaller than that for the YBCO + BSO(2.7). This is reasonable because the matrix structure and composition are degraded with increasing the BMO content. Furthermore, according to Fig. 3(c), the ε_{SF} strongly depends

on the Cu source, and compositional dispersion in films varied the ε_{SF} very sensitively, resulting in the variable spacing of stacking faults as observed in Fig. 1. Thus, the validity of the present energy analysis was confirmed. The present analysis demonstrates that the layered stacking fault structure in YBCO and nanocomposite strain have a dominant role in the present self-organization.

C. Temperature and oxygen pressure dependence of stacking fault formation

While the stacking faults were not formed during PLD, they were formed by the post–*ex situ* annealing. The reason for this is discussed in this section. According to a phase diagram of Y-Ba-Cu-O, the $YBa_2Cu_3O_7$ (YBCO) phase is more stable in high temperatures and low oxygen pressures, whereas the $YBa_2Cu_4O_8$ phase is more stable in low temperatures and high oxygen pressures [22]. Thus, the thermodynamic stability of stacking faults depends on temperature and oxygen pressure. The DFT gives the internal energy at 0 K, and the DFT is sufficient for "rough estimation" of ε_{SF} for the confirmation of validity in the present energy analysis. However, the Gibbs free energy analysis for ε_{SF} is needed in more quantitative analysis, and the phase diagram suggests that $\varepsilon_{SF}(x = 0) < 0$ for $T < \sim 750\,^{\circ}\mathrm{C}$ and $\varepsilon_{SF}(x = 0) > 0$ for $T > \sim 750\,^{\circ}\mathrm{C}$ at atmospheric pressure. Thus, if we consider the temperature and oxygen pressure dependences of ε_{SF}, we can explain that the stacking faults were formed at the *ex situ* annealing condition (low temperature and high oxygen pressure), not during PLD (high temperature and low oxygen pressure).

V. SUMMARY

The highly strained YBCO + BMO nanocomposite films were *ex situ* annealed to observe the self-organization of the long stacking faults with a spacing of 5–30 nm and a length of >500 nm. The TEM clarified that the stacking faults consisted of $Cu_{1-x}O$ chains. The XRD demonstrated that the *c*-axis length, namely, elastic strain, was reduced by the stacking fault formation. The strain energy analysis considering elastic strain, stacking faults, and accompanying dislocations clarified that the self-organization minimized the strain energy. Thus, the nonlocal nature of the present self-organization originated from the layered structure of YBCO stacking faults, and the large nanocomposite strain. The combination of nanocomposite strain and complicated defects in complex oxides can realize the nonlocal self-organization which is not observed in the conventional semiconducting films with epitaxial strain and misfit dislocations.

ACKNOWLEDGMENT

This work was partially supported by Grant-in-Aid for Scientific Research (B) (Grants No. 18H01478 and No. 18H01712).

[1] C. P. Kuo, S. K. Vong, R. M. Cohen, and G. B. Stingfellow, J. Appl. Phys. **57**, 5428 (1985).
[2] K. Brunner, Rep. Prog. Phys. **65**, 27 (2002).
[3] L. B. Freund and S. Suresh, *Thin Film Materials* (Cambridge University Press, Cambridge, 2003).
[4] J. P. Locquet, J. Perret, J. Fompeyrine, M. Machler, J. W. Seo, and G. V. Tendeloo, Nature **394**, 453 (1998).
[5] H. Y. Hwang, Y. Iwasa, M. Kawasaki, B. Keimer, N. Nagaosa, and Y. Tokura, Nat. Mater. **11**, 103 (2012).
[6] J. L. MacManus-Driscoll, Adv. Funct. Mater. **20**, 2035 (2010).
[7] H. Zheng, J. Wang, S. E. Lofland, Z. Ma, L. M. Ardabili, T. Zhao, L. S. Riba, S. R. Shinde, S. B. Ogale, F. Bai, D. Viehland, Y. Jia, D. G. Schlom, M. Wuttig, A. Roytburd, and R. Ramesh, Science **303**, 661 (2004).
[8] S. A. Harrington, J. Zhai, S. Denev, V. Gopalan, H. Wang, Z. Bi, S. A. T. Redfern, S. H. Baek, C. W. Bark, C. B. Eom, Q. Jia, M. E. Vickers, and J. L. MacManus-Driscoll, Nat. Nanotechnol. **6**, 491 (2011).
[9] J. L. Macmanus-Driscoll, P. Zeerrer, H. Wang, H. Yang, J. Yoon, A. Fouchet, R. Yu, M. G. Blamire, and Q. Jia, Nat. Mater. **7**, 314 (2008).
[10] T. Horide, F. Kametani, S. Yoshioka, T. Kitamura, and K. Matsumoto, ACS Nano **11**, 1780 (2017).
[11] E. D. Specht, A. Goyal, J. Li, P. M. Martin, X. Li, and M. W. Pupich, Appl. Phys. Lett. **89**, 162510 (2006).
[12] S. H. Wee, E. D. Specht, C. Cantoni, Y. L. Zuev, V. Maroni, W. Wong-Ng, G. Liu, T. J. Haugan, and A. Goyal, Phys. Rev. B **83**, 224520 (2011).
[13] C. Cantoni, D. T. Verebelyi, E. D. Specht, J. Budai, and D. K. Christen, Phys. Rev. B **71**, 054509 (2005).
[14] W. Y. Wang, Y. L. Tang, Y. L. Zhu, J. Suriyaprakash, Y. B. Xu, Y. Liu, B. Gap, S. W. Cheong, and X. L. Ma, Sci. Rep. **5**, 16097 (2015).
[15] R. Guzman, J. Gazquez, V. Rouco, A. Palau, C. Magen, M. Varela, J. Arbiol, X. Obradors, and T. Puig, Appl. Phys. Lett. **102**, 081906 (2013).
[16] T. Horide, K. Taguchi, K. Matsumoto, N. Matsukida, M. Ishimaru, P. Mele, and R. Kita, Appl. Phys. Lett. **108**, 082601 (2016).
[17] A. Llordes, A. Palau, J. Gazquez, M. Coll, R. Vlad, A. Pomar, J. Arbiol, R. Guzman, S. Ye, V. Rouco, F. Sandiumenge, S. Ricart, T. Puig, M. Varela, D. Chateigner, J. Vanacken, J. Gutierrez, V. Moshchalkov, G. Deutscher, C. Magen *et al.*, Nat. Mater. **11**, 329 (2012).
[18] J. Gazquez, R. Guzman, R. Mishra, E. Bartolome, J. Salafranca, C. Magen, M. Varela, M. Coll. A. Palau, S. M. Valvidares, P. Gargiani, E. Pellegrin, J. Herrero-Martin, S. J. Pennycook, S. T. Pantelides, T. Puig, and X. Obradors, Adv. Sci. (Weinheim, Germany) **3**, 1500295 (2016).
[19] K. Kishio, J. Shimoyama, T. Hasegawa, K. Kitazawa, and K. Fueki, Jpn. J. Appl. Phys. **26**, L1228 (1987).
[20] T. Horide, T. Kitamura, A. Ichinose, and K. Matsumoto, Jpn. J. Appl. Phys. **53**, 083101 (2014).
[21] See Supplemental Material at http://link.aps.org/supplemental/10.1103/PhysRevMaterials.3.013403 for XRD result of YBCO+BSO, Analysis of stacking fault spacing with varying parameters.
[22] J. Karpinski, H. Schwer, K. Conder, G. I. Meijer, E. Kopnin, and R. Molinski, Solid State Ionics **101–103**, 985 (1997).